Electronic Supporting Information

Utilizing MOF Precursors toward One-Step, Calcination-Free Synthesis of MnO_2 Superstructure for Superior Lithium Storage

Yang Fan,[a] Deli Luo,[a] Yan Wu,[a] Tianlang Peng,[a] Qi Qi,[a] Xubing Han,[a] Jinxin Zhou,[a] Yanling Wang,[c] Bao Lin,[a] Qinqin Xiong,[a] Yongjun Yuan,[a] Haiying Qin,a and Xiaoshi Hu[a,b]*

[a]Key Laboratory of Novel Materials for Sensor of Zhejiang Province and New Energy Materials Research Center, College of Materials and Environmental Engineering, Hangzhou Dianzi University, Hangzhou, 310018, PR China.

[b]State Key Laboratory of Silicon Materials, School of Materials Science & Engineering, Zhejiang University, Hangzhou, 310027, PR China

[c]Colledge of Information Engineering & Art Design, Zhejiang University of Water Resources and Electric Power, Hangzhou, 310018, PR China

* Corresponding author.

E-mail addresses: xshu@hdu.edu.cn (X. S. Hu); huxiaoshi.happy@163.com (X. S. Hu)

Supporting Figures and Table

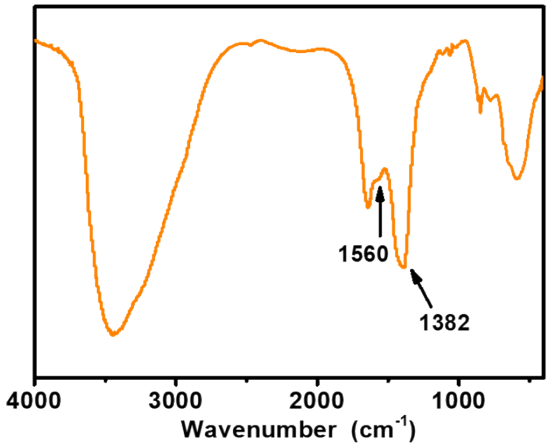

Fig. S1 FTIR spectrum of the the powder sample obtained by drying the filter liquor after reaction. It can be seen that obvious symmetric and asymmetric stretching vibrations of the carboxylate group situated at 1560 and 1382 cm^{-1} assigned to released $dobdc^{4-}$ linker from $Mn_2(dobdc)$ were present in the spectrum.[1]

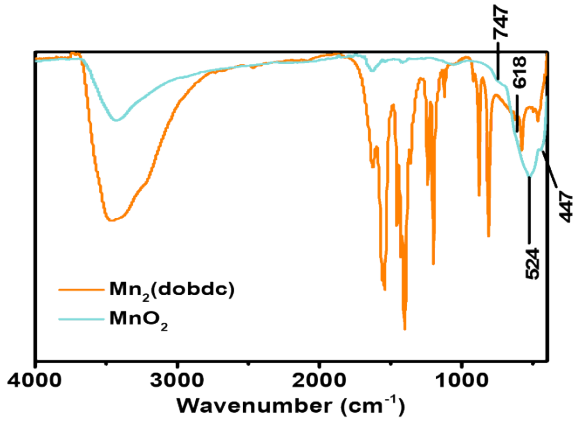

Fig. S2 Comparison of FTIR spectrum of $Mn_2(dobdc)$ precursor and synthesized MnO_2 materials. For MnO_2 material, the peaks at about 3425 cm^{-1} and other appreciable week bands above 800 cm^{-1} can be assigned to H–O–H stretching vibration and bending vibration of physically adsorbed water molecules by the MnO_2 products. The MnO_2 shows the absorptions at around 747, 618, 524 and 447 cm^{-1} peaks which are due to the Mn–O–Mn asymmetric stretching vibration and bending vibration mode. It can be seem that all the vibrations assigned to inoized $dobdc^{4-}$ linker of $Mn_2(dobdc)$ in the 400-1590 cm^{-1} region almost disappeared, suggesting that the organic portion of the framework had been completely consumed.[1, 2]

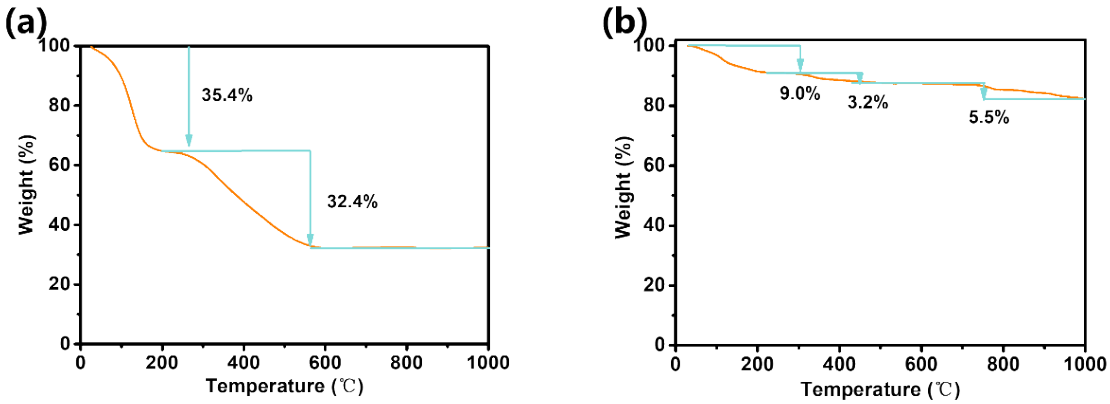

Fig. S3 TGA curves of (A) Mn_2(dobdc) and (B) MnO_2 samples in air. For the Mn_2(dobdc) sample, the mass loss of 35.4% blow 240 °C is related to the loss of coordinated solvent molecules and adsorbed water, while the weight loss of 32.4% in range of 300-600 °C stands for the decomposition of the $dobdc^{4-}$ ligands. No obvious weight loss is detected over 600 ℃, suggesting the complete decomposition of the framework to manganese oxides. For the MnO_2 samples, a weight loss of 9.0 wt.% below 240 °C is attributed to the loss of surface and interlayer water. The weight loss of 3.2 wt.% in the range of 320-600 °C is due to the change from MnO_2 to Mn_2O_3. The weight loss of 5.5wt.% occurs at over 600 °C is mainly due to the change from Mn_2O_3 to Mn_3O_4. [3, 4]

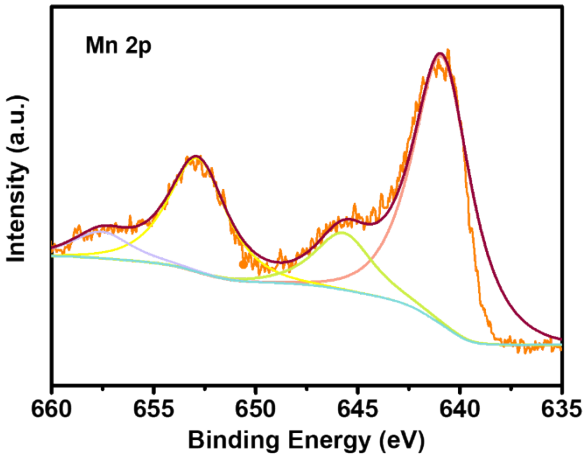

Fig. S4 High resolution XPS spectra for Mn 2p region measured for Mn_2(dobdc). The high-resolution XPS spectra of Mn 2p exhibit two peaks at 640.9 and 652.8 eV, which are corresponded to the Mn 2p3/2 and Mn 2p1/2 spin-orbit. The spin orbital splitting ΔE (Mn2p3/2- Mn 2p1/2) of 11.9 eV can be assigned to the Mn^{2+}.[5]

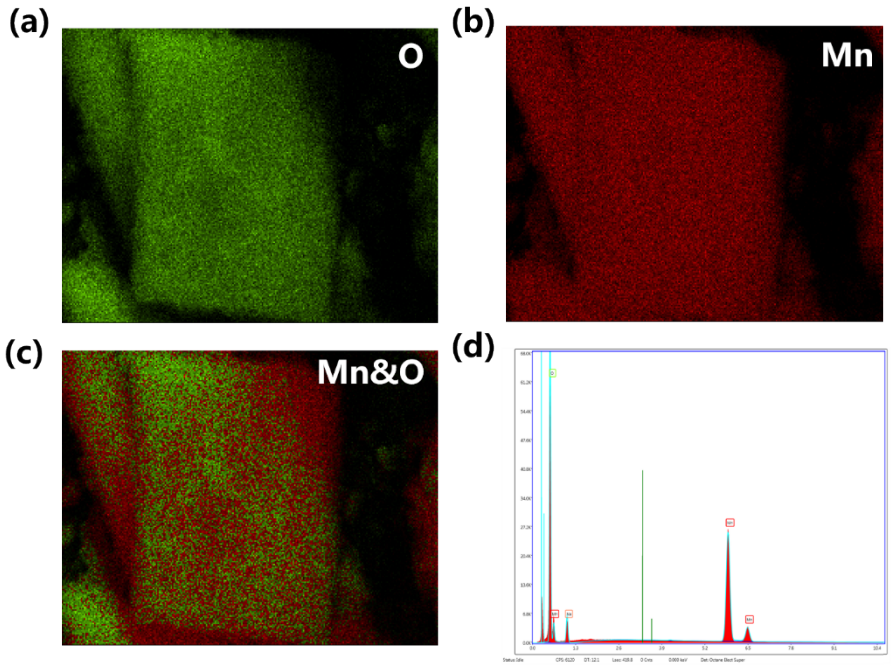

Fig. S5 EDX analysis of hierarchical mesoporous MnO_2 polyhedron particle: (A) O, (B) Mn and (C) Mn&O elemental mapping images of single particle, and (D) EDX spectra.

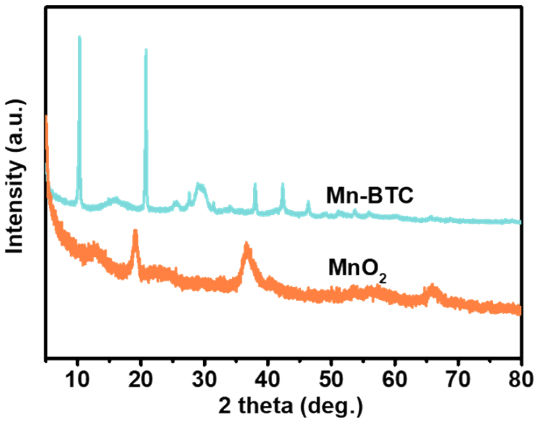

Fig. S6 XRD of rod-shaped Mn-BTC MOF precursors synthesized by following a modified literature method[6] (the amount of all raw materials were magnified five times in our modified synthesis with other conditions kept constant) and its derived MnO_2 product.

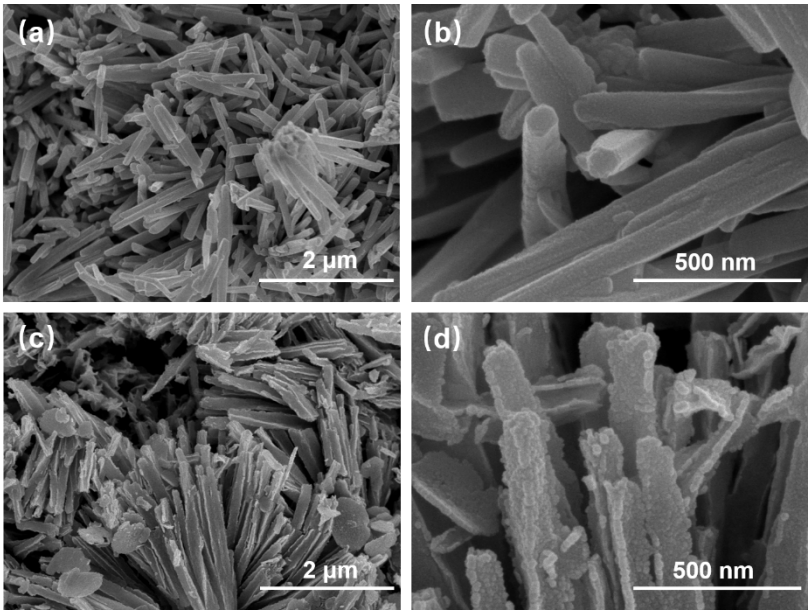

Fig. S7 SEM images of (a, b) rod-shaped Mn-BTC MOF precursors and (c, d) its derived MnO_2 product.

Table S1. Comparison of cycling performance of this work with other reported MnO_2-related anode materials.

Sample	**Rate(mA g^{-1})**	**Retention capacity (mA h g^{-1})**	**Cycle number**	**Ref.**
Hollow MnO_2 nanospheres	100	840	60	[7]
α-MnO_2 nanotubes	200	618	300	[8]
3D hierarchical MnO_2 microspheres	300	715	200	[9]
α-MnO_2 hollow urchins	270	481	40	[10]
MnO_2 Nanowires	85	710	50	[11]
Three dimensional hierarchically porous crystalline MnO_2	400	778	200	[12]
Core-shell porous MnO_2/Carbon nanosphere composite	300	604	200	[13]
MnO_2 nanoflakes on vertically aligned carbon nanotubes	250	803	150	[14]
MnO_2 nanowire/graphdiyne	200	660	120	[15]
MnO_2/3D porous graphene-like composites	100	836	200	[16]
MnO_2-coated carbon nanohorns	100	705	60	[17]
Core-shell MnO_2/3D-ordered hollow carbon sphere composite	100	692.5	100	[18]
Nanoflaky MnO_2/carbon nanotube nanocomposites	200	620	50	[19]
Hierarchically layered mesoporous MnO_2 micropolyhedron	200 1000	866 797	60 300	This work

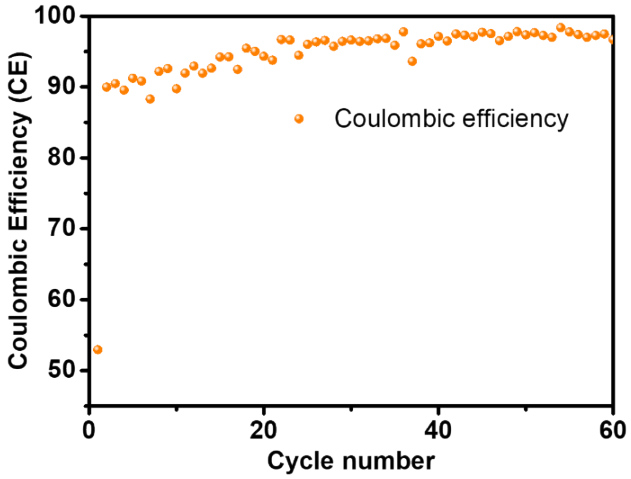

Fig. S8 Coulombic efficiency of the MnO_2 electrode when cycled at 200 mA g^{-1}.

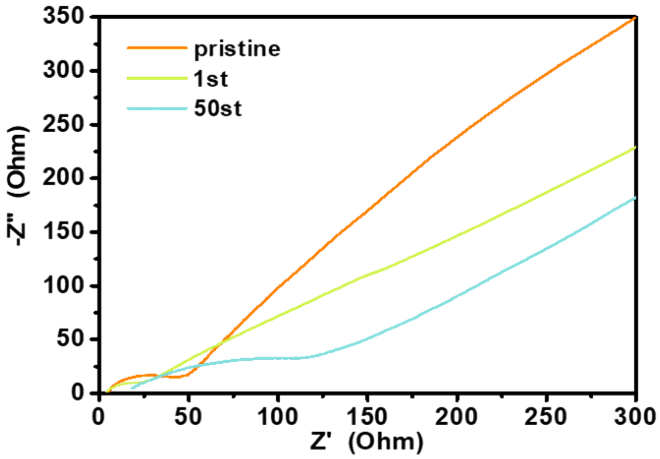

Fig. S9 Nyquist plots of our MnO_2 anode at the pristine state, after 1 cycle and after 50 cycles, respectively.

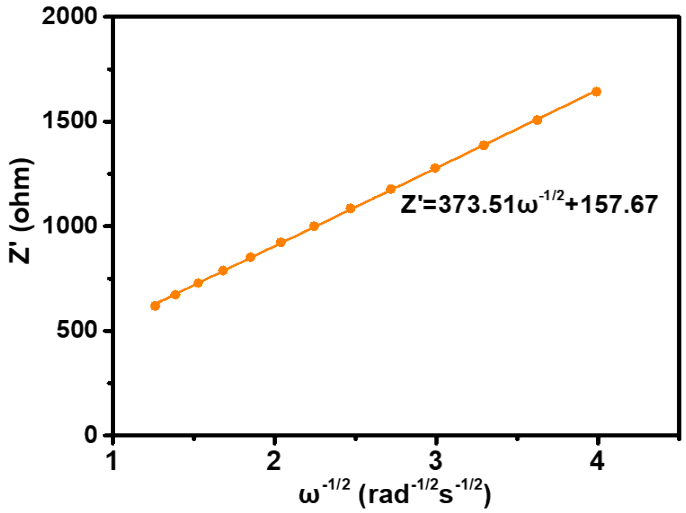

Fig. S10 Relationship between Z' and $\omega^{-1/2}$ for the MnO_2 electrode after 50 cycles, the slope of the fitting line can be adopted to calculate the ion diffusion coefficient. The Li-ion diffusion coefficient (D) in the electrode complies with the following formulas:[20]

$D=(R^2T^2)/(2A^2n^4F^4C^2\sigma^2)$ (1)

$Z'=\sigma\omega^{-1/2}$ (2)

where R, T, A, n, F, C, and σ correspond to gas constant (8.314 J mol^{-1} K^{-1}), absolute temperature (298 K), electrode area (1.77 cm^2), electron transfer number per formula (ca. 4), Faraday constant (96485 C mol^{-1}), concentration of Li-ions (1×10^{-3} mol cm^{-3}), and Warburg factor respectively. The Warburg factor σ can be obtained after fitting the slope of Z′ versus $\omega^{-1/2}$ and was determined to be 373.51.

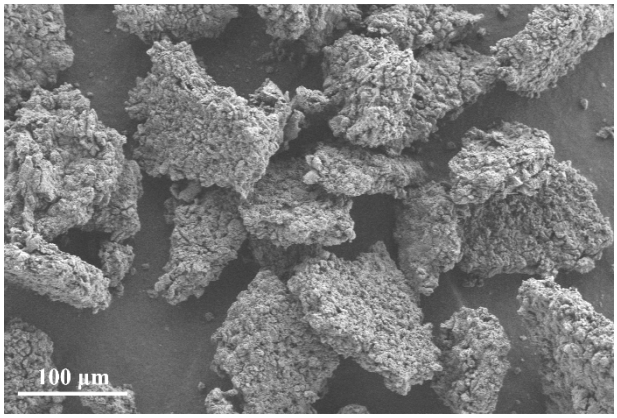

Fig. S11 Panoramic SEM images of MnO_2 electrodes at charged state after long-term cycling.

Supplementary references

[1] C. Feng, S. S. Qiao, Y. Guo, Y. H. Xie, L. Zhang, N. Akram, S. A. Li and J. D. Wang, Colloids Surf, A, 2020, **597**, 124781.
[2] N. D. Kim, H. J. Yun, I. K. Song and J. Yi, Scr. Mater., 2011, **65**, 448-451.
[3] X. M. He, J. J. Li, Y. Cai, C. Y. Jiang and C. R. Wan, Mater. Chem. Phys., 2006, **95**, 105-108.
[4] J. Petlicki,,D. Petlicki and T. G. van de Ven, Ind. Eng. Chem. Res., 2005, **44**, 2002-2010.
[5] X. B. Feng, C. W. Chen, C. He, S. N. Chai, Y. K. Yu and J. Cheng, J. Hazard. Mater., 2020, **383**, 121143.
[6] F. C. Zheng, G. L. Xia, Y. Yanga and Q. W. Chen, Nanoscale, 2015, **7**, 9637-9645.
[7] J. Yue, X. Gu, L. Chen, N. N. Wang, X. L. Jiang, H. Y. Xu, J. Yang and Y. T. Qian, J. Mater. Chem. A, 2014, **41**, 17421-17426.
[8] L. H. Li, C. Y. Nan, J. Lu, Q. Peng and Y. D. Li, Chem. Commun., 2012, **55**, 6945-6947.
[9] S. Khalid, C. B. Cao, M. Naveed and W. Younas, Sustainable Energy Fuels, 2017, **8**, 1795-1804.
[10] B. X. Li, G. X. Rong, Y. Xie, L. F. Huang and C. Q. Feng, Inorg. Chem., 2006, **45**, 6404-6410.
[11] M. S. Wu and P.-C. J. Chiang, Electrochem. Commun., 2006, **8**, 383-388.
[12] S. K. Liu, X. S. Liu, J. P. Zhao, Z. Q. Tong, J. Wang, X. X. Ma, C. X. Chi, D. P. Su, X. X. Liu and Y. Li, RSC Adv., 2016, **6**, 85222-85229.
[13] Z. G. Cao, Y. B. Yang, J. L. Qin and Z. X. Su, J. Power Sources, 2021, **491**, 229577.
[14] A. Abdollahi, A. Abnavi, F. Ghasemi, S. Ghasemi, Z. Sanaee and S. Mohajerzadeh, Electrochim. Acta, 2021, **390**, 138826.
[15] Y. D. Lin, H. F. Kang, M. X. Liang, X. X. Ye, J. X. Li, Q. Feng, Y. P. Zheng and Z. G. Huang, Appl. Surf. Sci., 2020, **526**, 146457.
[16] Y. Y. Li, Q. W. Zhang, J. L. Zhu, X. L. Wei and P .K. Shen, J. Mater. Chem. A, 2014, **2**, 3163-3168.
[17] H. Lai, J. X. Li, Z. G. Chen and Z. G. Huang, ACS Appl. Mater. Interfaces, 2012, **4**, 2325-2328.
[18] J. Zang J. J. Chen, C. L. Zhang, H. Qian, M. S. Zheng and Q. F. Dong, J. Mater. Chem. A, 2014, **2**, 6343-6347.
[19] H. Xia, M .O. Lai and L. Lu, J. Mater. Chem., 2010, **20**, 6896-6902.
[20] C. Li, X. S. Hu, W. Tong, W. S. Yan, X. B. Lou, M. Shen and B. W. Hu, ACS Appl. Mater. Interfaces, 2017, **9**, 29829-29838.